Characterisation of hidden defects using the near-field ultrasonic enhancement of Lamb waves

A.R. Clough, R.S. Edwards

Department of Physics, University of Warwick, Coventry, CV4 7AL

Abstract

Defects that propagate from the inside of a structure can be difficult to detect by traditional non-destructive inspection methods. A non-contact inspection method is presented here that uses the near-field interactions of ultrasonic Lamb waves to detect defects propagating into a 1.5 mm thick aluminium sheet from the opposite side to that which is inspected. Near-field interactions of the S0 Lamb waves with the defects are shown to give rise to a characteristic increase in the wave magnitude, which is used to position and characterise these hidden defects. It is shown that such defects are difficult to detect from a study of their influence on ultrasonic transmission alone. Single defects of different depths, and systems of multiple defects with varying separations and relative depths, are successfully detected in both experimental trials and FEM simulations. Reliable single defect detection is achieved for defects with a minimum depth of 30% of the plate thickness, and resolution of multiple defects is achieved for defect separations of 5 mm.

Keywords: Lamb Waves, Scanning Laser Detection, Stress Corrosion Cracking, Enhancement

1. Introduction

Early detection of cracking in industrial applications allows replacement of the faulty part, preventing component failures which are costly both in economic and environmental terms[1]. Surface-breaking cracks, such as defects caused by stress-corrosion cracking (SCC), in which defect growth occurs when a material is placed under stress in a corrosive environment, are of concern in industrial pipework and chemical storage systems[1–4]. SCC defects typically have a size scale of several millimetres with a complicated branched structure, and can occur singly or in groups of defects located close together[1].

Such defects are traditionally detected using dye penetrant inspection, however, the application of this technique requires extended downtime of the system under test as the inspection cannot be done during operation[5,6]. Dye penetrant inspection also requires direct access to the damaged surface and so success is limited when access to the object under test is restricted. Radiographic inspection can also be employed to detect these types of defects, however, safety concerns arising from the use of ionising radiation can limit the application in industrial settings[7].

Email address: r.s.edwards@warwick.ac.uk (R.S. Edwards)

Ultrasonic inspection is an attractive alternative to dye penetrant inspection, however, conventional piezoelectric ultrasonic transducers require the use of couplant, and as such have a limited capacity for scanning large samples or at elevated temperatures[4,8–10]. The use of non-contact ultrasonic generation and detection methods, such as laser ultrasonics[11] and electromagnetic acoustic transducers (EMATs)[12] removes the need for couplant, and thereby provides the potential to perform simple scanning inspections on components[13].

The use of ultrasonic waves with displacements throughout the thickness of a material, such as Lamb waves in sheets and guided waves in pipes[14,15], enables inspection of areas of the system that cannot be accessed directly, such as the internal surface of a pipe[8,16]. Several long-distance ultrasonic inspection methods exist that monitor in the defect far-field (defined as the region starting at a distance of several wavelengths away from the defect[17]) through changes in the reflection or transmission of guided waves as they interact with surface-breaking defects, and these methods are capable of estimating the position and depth of defects over a distance of several metres[8,9]. However, the reflectivity of small, shallow defects is low, which restricts the size of defects that can be detected by this far-field approach. The am-

plitude of the wave that is transmitted past a defect can also be used to estimate depth; a larger reduction in amplitude indicates a deeper defect[18]. However, when the defect is very small or not orientated perpendicular to the direction of wave propagation, detection can be difficult to achieve for a detector located far away from the defect, as diffraction around the defect can prevent changes in transmission from being observed[8].

In addition, SCC defects are not a singular occurrence and often multiple defects occur in a component, each of which may grow to a different depth[1]. Interaction of ultrasonic guided waves with these clusters of defects offers significant complexity to the measurements, for example due to the reduced amplitude for reflected waves from later defects. Interactions therefore tend to be dominated by the relative depth of the defect that is first encountered by the incident wave, and the defect separation[19], with overall transmission tending to be dominated by the deepest defect[18].

An alternative to these far-field studies is the use of a scanning inspection system to monitor changes in the ultrasonic propagation as and when they occur, thereby minimising the influence of issues such as diffraction around small defects or low defect reflectivities[20–24]. The most distinctive near-field effect is the enhancement of an ultrasonic surface wave, which is observed when an ultrasonic source or detector is scanned directly over a defect (figure 1).

1.1. Near-field enhancements

The enhancement of surface waves has been observed for Rayleigh[20,21] and Lamb waves[22,23], for surface-breaking defects which propagate into the sample from the side which is inspected. When a detector is scanned over such a defect, constructive interference between the incident wave mode (Rayleigh or Lamb) and wave modes that are reflected and mode converted at the defect gives rise to a characteristic increase in the signal amplitude, and an increase in the magnitude of individual frequency components of the incident wave[20–22]. A similar mechanism is responsible for the enhancement when the ultrasonic source is passed over the defect, with additional contributions when using laser ultrasonics arising from changes in the boundary conditions and spatial profile of the laser generation source at the defect[21,23].

When using Lamb waves, mode conversion can occur between all of the wave modes that are supported at the frequency-thickness of inspection, with more modes available at higher frequency-thicknesses[22,25]. Following interaction, these waves propagate away from the defect with velocities determined by the mode (shown in figure 2), and enhancement is only observed close to the defect when these reflected and mode converted waves arrive within the same time window as the incident mode[22].

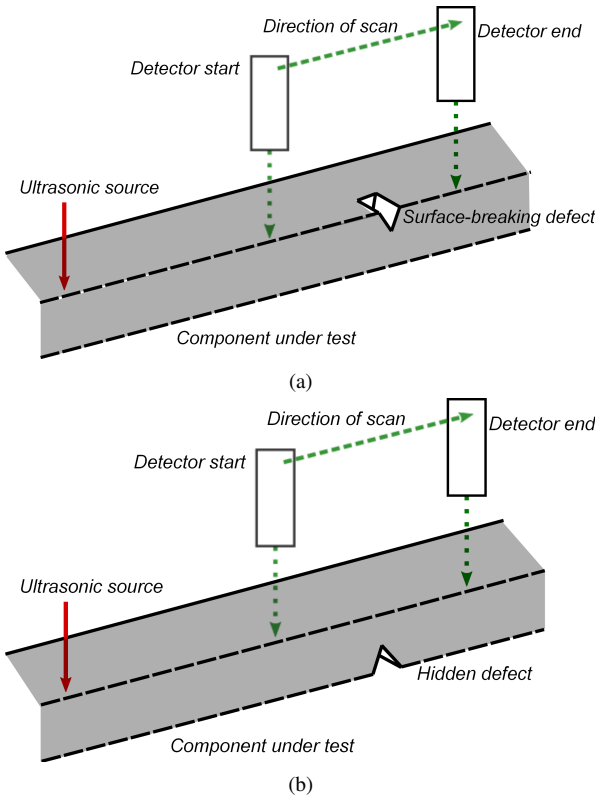

Figure 1: A cut-through of a sample showing scanning laser detection of the defect near-field in a sheet for defects on the same side as the inspection (a) and hidden defects (b).

The location at which the enhancement occurs can be used to determine the position of the defect[22,24]. In addition, the magnitude of the enhancement has been used to give an estimate of the severity of the defect, with a larger enhancement indicating a more severe defect due to the larger reflections[22–24]. The remote, non-contact nature of laser ultrasonics and EMAT inspection allows for the scanning inspection that is essential for these measurements, however, the high spatial resolution offered by laser ultrasonics makes it the ideal candidate for near-field inspection[24].

Previous studies have examined the enhancement of guided waves as the laser detector or source is passed over a surface-breaking defect that propagates into the surface of the material from the inspection side (figure 1a). However, many defects can propagate outwards

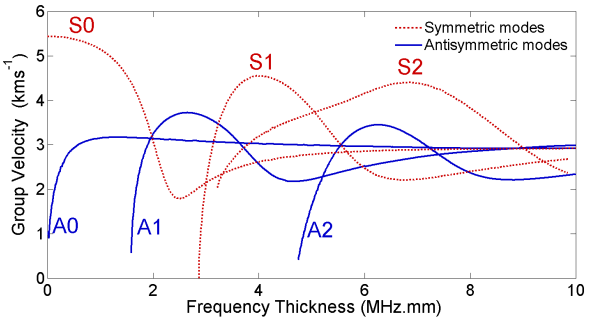

Figure 2: Lamb wave group velocity dispersion curve for aluminium.

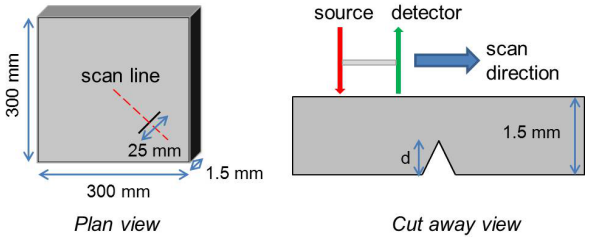

Figure 3: A schematic diagram showing scanning laser detection inspection of laser micro-machined defects of depth d in 1.5 mm thick aluminium sheets.

from the inside of a structure, such as a pipe or storage tank, and leave no visible indication of the defect on the outer surface of the structure; this situation is similar to that shown in figure 1b. The present study identifies near-field ultrasonic enhancements arising from defects that propagate into the material from the far side of the structure, relative to the testing surface, and demonstrates how these enable positioning and characterisation of such hidden defects. The near-field interactions with multiple hidden defects, where two closely-spaced defects are present, are shown as the defect separation and the depths of the defects relative to one another are varied.

2. Methods

Inspections were performed on 1.5 mm thick aluminium plates (300 x 300 x 1.5 mm) into which artificial defects with a v-shaped side profile (figure 3) were cut by laser micro-machining. Defects of length 25 mm and of different depths, d, were produced (ranging from $5\% \leq d \leq 100\%$ of the through-thickness of the sheet) at a position such that reflections from the sheet edges were minimised. The v-shaped profile was chosen as a simplified representation of the opening part of a SCC defect, and the average defect opening width was $282 \pm 16\mu$m. Inspection in the near-field of the defect was carried out by scanning both the source and detection lasers over the undamaged side of the plate such that the detector passed over the defect region. The scanning was performed using a linear stage with a scan step of 0.05 mm.

Generation of ultrasound used a pulsed Q-switched Nd:YAG laser (1064 nm wavelength, 10 ns rise time), operating in the thermoelastic regime to limit sample damage, focused to a spot with 2 mm diameter to give a broadband ultrasonic source with significant frequency content in the range of 0.1 - 6 MHz[11]. Both symmetric and antisymmetric Lamb waves were excited, with velocities dependent on the frequency of the excitation and the thickness of the sheet[25]. Detection of ultrasound was carried out using a two-wave mixing interferometer (1550 nm wavelength) from Intelligent Optical Systems (IOS)[26], which provides a measure of the out-of-plane displacement on the material surface. The IOS detector has a spot size of 200 μm, allowing for high spatial resolution when scanning. The generation and detection lasers were held at a fixed separation in order to simplify the interpretation of the multi-modal ultrasonic signals received, and to minimise the influence of attenuation[22,23].

In addition to the experimental measurements, a series of 3D finite element method simulations were carried out using PZFlex. Simulated v-shaped defects of different depths in 1.5 mm thick sheets were studied by using a dipole force located a fixed distance away from the defect to simulate the laser generation. The out-of-plane displacement at the nodes on the undamaged side of the sheet, for a line passing over the mid-point of the defect, was recorded in a similar fashion to the experimental data. A fixed separation was not maintained in the simulation as the calculation of new boundary conditions at each new source location is very time consuming. The element spacing in the FEM simulations was 0.1 mm.

3. Results

3.1. Single defect

A-scans were recorded at each scan position and adjacent scans were stacked to form B-scans, with an example B-scan shown in figure 4 and A-scans in the lower panels of figure 5. Negative detector position on the B-scan corresponds to both the detector and generator positions being on the same side of the defect, prior to in-

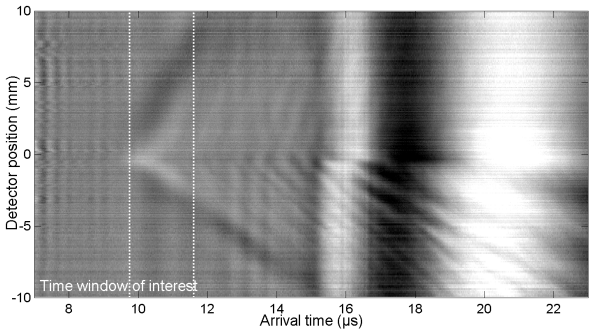

Figure 4: A B-scan image for an experimental scan across a 100% through-thickness defect located at 0 mm. The time window used to monitor enhancements is shown by the region bounded by dashed lines.

teraction (measuring incident and reflected waves); positive detector positions here correspond to the generator and detector being on opposite sides of the defect (measuring transmission). The scan was performed perpendicular to the defect, as shown in figure 3, to simplify the analysis.

For the frequency-thickness region of interest, the only supported wavemodes are the S0 and A0 waves. These are broadband with a central frequency of 1.05 MHz, and the exact arrival times depend on the velocity for each frequency (figure 2)[25]. Incident S0 and A0 modes have constant arrival time during the scan (figure 4). Reflected and mode converted waves have a varying arrival time, with several such waves visible on the B-scan. When the incident S0 mode interacts with the defect it will undergo several processes; reflection of the incident wave to produce a backwards travelling S0 wave, transmission forwards under the defect, and mode conversion to other modes that are supported at the same frequency-thickness, in this case an A0 wave, which will propagate both forwards and backwards from the defect[22,28,29]. These interactions are shown schematically in figure 6.

Full identification of the wavemodes present requires use of time-frequency techniques to identify overlapping modes. However, by taking the central frequency as being dominant, an approximate identification of the waves on figure 4 is possible. For the central frequency velocities are 5110.1 ms^{-1} for the A0 mode and 3160.9 ms^{-1} for the S0. The incident and transmitted S0 modes arrive at approximately 10 μs, with low amplitude (these have predominantly in-plane motion[25], while the detection system is sensitive to out-of-plane displacements). In the negative position region, corresponding to incident and reflected waves, a

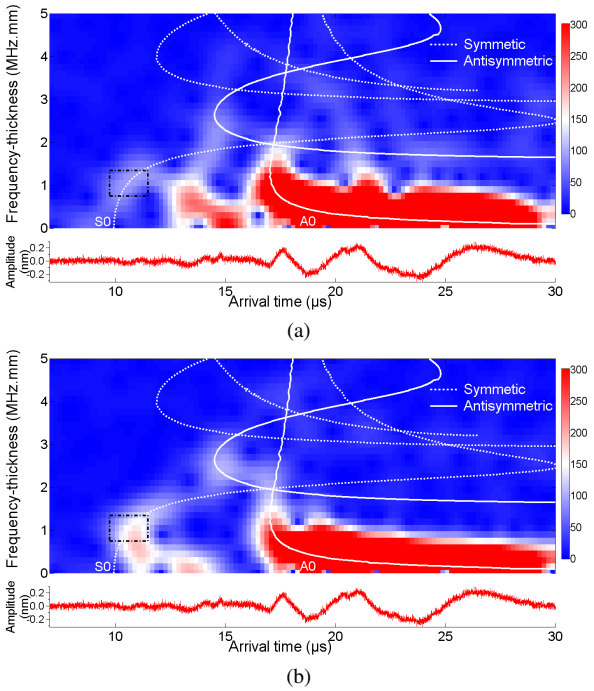

Figure 5: A-scans (lower panels) and time-frequency representations (upper panels) taken on a defect free sheet (a) and for a 75% through-thickness defect for a detector position of 0.05 mm prior to the defect (b), shown overlain with theoretical arrival times of Lamb waves. The region of interest of the S0 mode is highlighted.

strong mode-converted S0-A0r mode is observed, arriving a time $\Delta t_{S0-A0r} = |x|(1/v_{A0} + 1/v_{S0})$ after the incident S0 wave, where v_{A0} is the velocity of the A0 mode, v_{S0} is the velocity of the S0 wave, and x is the detector position relative to the defect. A weaker S0-S0r is also observed, but with much smaller amplitude due to being primarily in-plane. Following transmission (positive detector positions) the S0-S0 transmitted mode continues to arrive at around 10 μs. However, the arrival time of the S0-A0 transmitted mode varies depending on the distance of the detector from the slot (and hence how far the wave propagates as an S0 and as an A0 wave), with the time-varying arrival time occurring a time $\Delta t_{S0-A0t} = x(1/v_{A0} - 1/v_{S0})$ after the S0-S0 transmitted wave. The defect position is shown by the point at which these reflected and mode-converted waves originate (detector position of 0 mm).

Individual Lamb modes and their frequency-dependent behaviour can be fully identified by using a sonogram time-frequency representation, which is

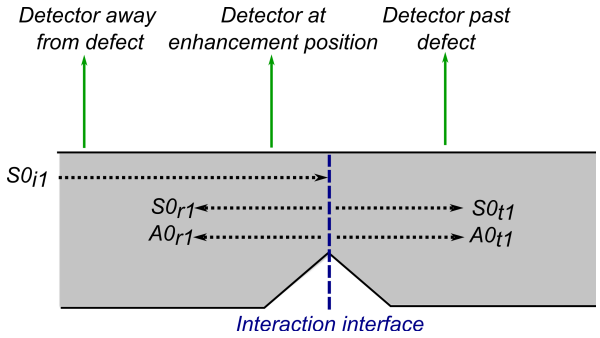

Figure 6: Interactions of the incident S0 wave encountering a hidden v-shaped defect. Subscript *i* corresponds to an incident wave, *r* is a reflected wave produced at the defect, and *t* is a wave transmitted past the defect.

created by splitting the time-domain data into many equal sized sections and producing a Fourier transform of each[27]. The theoretical arrival times of individual modes are overlain onto the sonograms to enable identification of modes, producing figures such as figure 5[22,23].

Initial investigations were carried out on sheets that contained a single isolated defect, with experiments and simulations performed with the detector scanned across the undamaged side of the sheet, as shown in figure 1b. Enhancements were observed at several frequencies and arrival times on the sonograms, corresponding to interactions of different modes with the defects; see, for example, the increased magnitude in the windowed region of figure 5a compared to that on figure 5b. Enhancement of the S0 mode was chosen for full analysis as it corresponds to the earliest arriving incident Lamb wave at the detector, arriving at approximately 10 μs in figure 4, and it can, therefore, be studied without interference from other modes in a defect free sheet. For a sheet containing defects, any changes that occur in this region are caused by interactions between the incident S0 wave and those waves reflected and mode converted at the defect.

The maximum magnitude of the sonogram was measured in a chosen region corresponding to the incident S0 mode, at frequency-thicknesses between 0.75 - 1.35 MHz.mm, and arrival times (for the fixed experimental source to detector separation) between 9.75 - 11.6 μs. This region is shown by the dashed box on figure 5. By tracking the peak magnitude in this region during a scan, variations in the chosen wavemode can be identified. This variation in the magnitude has previously been used to characterise the 'amount' of that wave which is present at a given detector position[22–24].

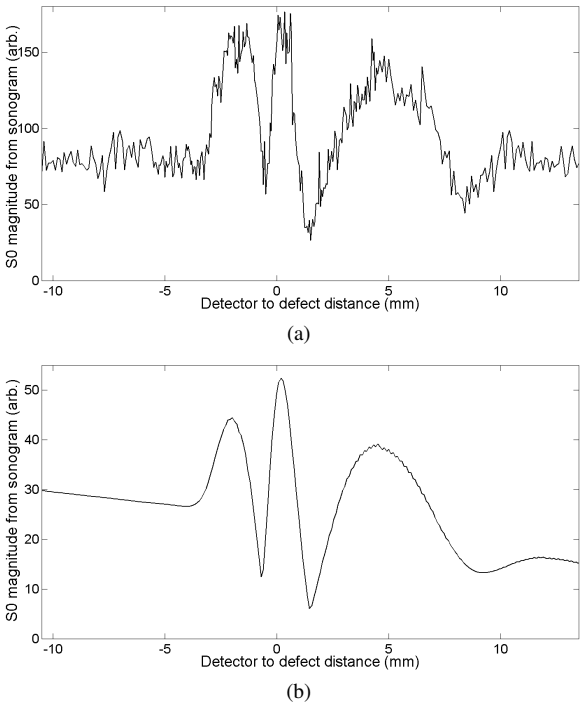

Figure 7: Variation in the sonogram magnitude of the S0 wave in the chosen region as a function of detector position for experimental (a) and simulated (b) scans over a hidden defect with a depth of 50% of the sheet thickness.

An example of the variation of the magnitude during a scan for the chosen S0 wave, incident on a 50% through-thickness defect, is shown in figure 7 for experimental (a) and simulated (b) data.

In the experimental data (figure 7a), the left hand region has a steady average magnitude, showing that the magnitude comes from the incident wave only. The right hand region (where the source and detector are on opposite sides of the defect) shows the magnitude of the S0 wave returning to the pre-defect level due to diffraction underneath and around the defect, highlighting the difficulty in using changes in transmission to characterise small length defects when measuring in the far-field. The model data shows a similar behaviour, with an overall downward slope due to the spread of the wave front as the separation of generation and detection points increases.

When the detector is in the near-field of the defect, defined here as when the detector is within ±4 mm from the defect midpoint, interactions between reflected, transmitted and mode-converted waves occur. Between detector positions of -4 and 0 mm, the reflected and

mode converted waves arrive within the same time window as the incident S0 wave, leading to wave superposition and interference[22] (also shown on the B-scan, figure 4). In the region of the scan in which this interference occurs, the reflected and mode converted waves change arrival time and phase relative to the incident S0 wave as the distance to the defect changes[28,29], with regions of constructive and destructive interference observed. This is shown by the distinctive pattern of multiple enhancement peaks in figure 7. The enhanced signals are over twice the magnitude of the incident S0 wave and give a clear indication of the presence of a defect.

The interactions of the incident S0 mode with the defect are shown schematically in figure 6; this shows reflection of the incident wave to produce the reflected (backwards travelling) S0 wave, a transmitted (forward travelling) wave, and mode-conversion to other modes supported at this frequency thickness, in this case an A0 wave. This propagates both forwards and backwards from the defect, with the arrival times dependent on the velocities[22,25,28,29].

At certain points in the near-field, the phase difference between incident and reflected / mode-converted waves is small, giving constructive interference and an increased signal magnitude. At other points, the waves are out-of-phase with the incident wave mode, such that destructive interference can occur; this produces the drops in magnitude at a detector position of -1 mm in figure 7. The main enhancement peak (peak 1) is observed very close to 0 mm on the scan, where the modes interfere constructively; the second peak is observed at -2 mm when the reflected and mode converted waves again come into phase with the incident mode[22,25].

When the detector moves past the defect the waves that are present in the time window analysed are the transmitted S0 wave and the forward travelling mode converted A0 wave[28,29]. These interfere constructively, as before, giving rise to the broader peak centred around a detector position of 5 mm in figure 7a. Following transmission there is only a slow change in the relative phase difference between the two modes, allowing them to stay in phase over a longer distance; there is no path difference between transmitted S0 and A0, and the shape of the enhancement peak is due to the different velocities and phases of the modes.

To quantify the enhancement an enhancement factor E_f is calculated[22,23], and is found for the enhancement peaks shown at detector positions of -2 mm and 0 mm in figure 7. E_f is given by the ratio of the enhanced magnitude, $E_{Enhanced}$ (the peak magnitude), to the magnitude that is present when there is no defect, $E_{NoDefect}$ (taken from the far-field incident wave for the experiments, and considering the attenuation for the models),

$$E_f = \frac{E_{Enhanced}}{E_{NoDefect}} \quad . \tag{1}$$

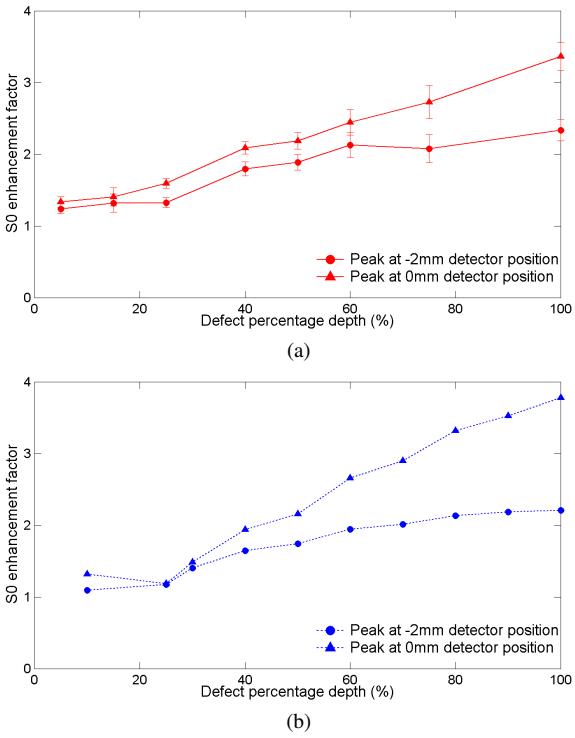

Figure 8: Variation in the enhancement factor of the S0 wave in the region of interest as a function of defect depth, for experimental (a) and simulated (b) scans over a single hidden defect.

The S0 enhancement factor is found to vary as a function of defect depth and is shown in figure 8 for enhancements measured at both positions. The enhancement factors increase with increasing defect depth for both experimental (figure 8a) and simulated data (figure 8b). This increasing enhancement factor is caused by the increase in the reflection coefficient of the S0 wave and the increase in the amount of mode conversion to A0 waves experienced at deeper defects[28,29]. The enhancements observed in the simulations are slightly larger than their experimental counterparts as they are recorded on a single point node, whereas the experimental data is averaged over the 200 μm diameter detector spot, but follow the same trend.

A measure of the severity of the hidden defect can be obtained from the magnitude of the enhancement factor. This can be assessed from either enhancement peak, as

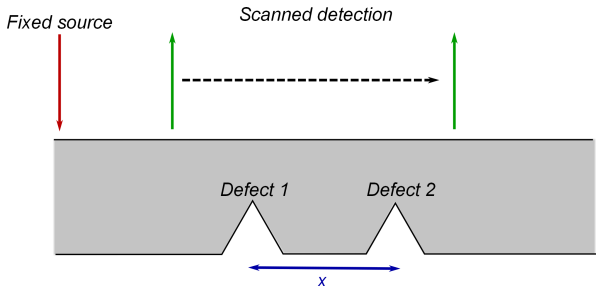

Figure 9: Set-up for FEM simulations on components containing multiple defects of fixed depth (50% of sheet thickness) separated by a distance x.

long as the choice of peak is consistent between inspections, or by considering both together to allow for variations in the reflection coefficient due to crack roughness. The pattern of the enhancement peaks shown in figure 7 is consistent between defects of different depth, and hence the hidden defect can be positioned by the location at which the central enhancement peak occurs. This is particularly important for the detection of hidden defects where there is no visible sign of a defect on the material surface.

3.2. Multiple defects

In many occurrences of SCC the material will develop defects at multiple locations[1]. Each crack will contribute to the failure of the component, and hence reliable detection and resolution of multiple hidden defects and a measure of their relative depths and positions is of interest.

Investigation into the near-field interactions between an incident S0 wave and multiple hidden defects was carried out using FEM simulations to allow investigation of a wide range of defect combinations. Figure 9 shows the simulation set-up used to investigate a pair of defects, both with a depth of 50% of the sheet thickness (1.5 mm), with separation x. This separation was varied between x = 0.2 mm (corresponding to when the two defects are effectively conjoined) and 12 mm. The same data processing procedure as for the single defects was performed, and the variation in the sonogram magnitude for each scan is shown in figure 10.

For small separations between the two defects (less than 1 mm) the pattern of near-field enhancement of the S0 wave is very similar in form to that of the single defect, with the first visible differences arising at a separation of 1 mm. At this separation the overall enhancement shows interference between two sets of near-field enhancements, both of which resemble the single defect

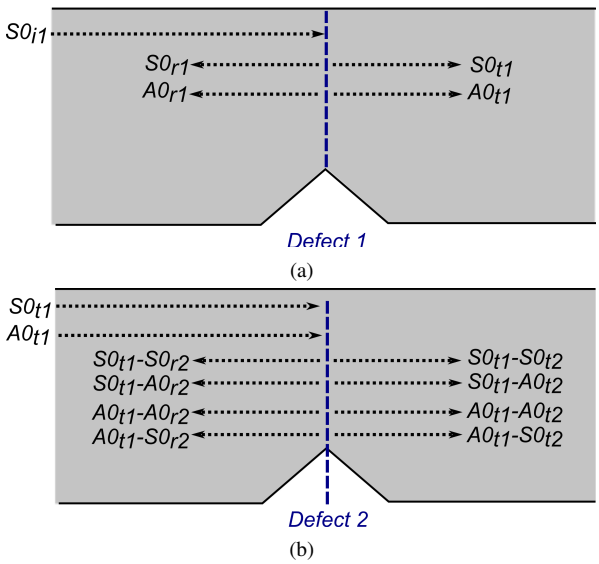

Figure 11: Interactions of the incident S0 wave with two hidden v-shaped defects of 50% depth.

shape, with a small offset from one another. The interference between these enhancements makes it difficult to determine the depths of the defects using the calibration obtained from the single defect measurements, however, it can be surmised from the pattern that the defect is more complex than a single defect. As the defect separation increases it becomes possible to resolve two clear near-field enhancements, each one associated with a defect, and for the 50% defects used here two separate enhancements are clearly resolvable for defect separations of 5 mm and larger.

The first enhancement follows the same mechanism as for a single defect. The second enhancement is created by the same interference mechanism, however, the wave incident on the second defect is comprised of the transmitted S0 wave and the forward travelling component of the mode converted A0 wave from the first defect, shown in figure 11. This leads to an increased complexity of the signal analysis when the defects are close together and both of these wavemodes arrive in the time window for analysis (i.e. the second enhancement lies on top of the peak following transmission, centred around 5 mm on figure 7). When the detector passes over the second defect these additional mode conversions must be considered, providing additional contributions to the enhancement[28,29], with interactions shown in figure 11b. These additional wave modes provide varying contributions to the enhancement as the separation increases, as the increased propagation distance leads to a varying phase difference with respect to the

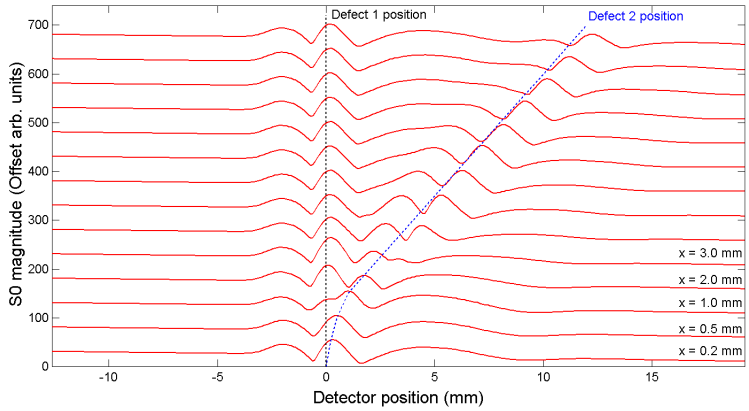

Figure 10: Variation in the sonogram magnitude of the studied S0 wave for two defects that are 50% of the through-thickness of the sheet, for increasing separation between the defects.

S0 wave of interest, meaning that at some positions their interactions will be more constructive in nature, and at other positions destructive. This will affect the analysis for defect separations of 7 mm or less (see velocities in figure 2 and the width of the enhancement peaks in figure 10).

For single defects the near-field enhancement varies with defect depth, and this variation can also be exploited in order to determine the depths of multiple defects relative to one another for certain separations. The near-field enhancement of the S0 wave was examined for two different defect separations, x = 1 mm and x = 5 mm, for varying depths, giving poorly resolved (1 mm) and almost resolved defects (5 mm). One of the defects was fixed at 50% of the sheet thickness and the other defect was varied in depth, between 10% and 90% of the sheet thickness, with the detection encountering the 50% defect first (figures 12a and 13a for 1 mm and 5 mm separations respectively), or second (figures 12b and 13b).

Figures 12a and 12b (separation of 1 mm) show small variations in the structure of the enhancement peaks when compared to those for a single defect (figure 7b), with the behaviour dominated by the larger defect in each case. Once the correct enhancement peaks are identified, a general trend in the behaviour is again observed, with larger enhancements with increasing defect depths.

The increasing enhancement with defect depth when the deeper defect is encountered first is due to the increased contribution to the enhancement from the $A0_{r1}$ and $S0_{r1}$ waves (figure 11a) as the defect depth increases, as for the single defect case [22,28,29]. This leads to a subsequent decrease in the magnitude of the $S0_{t1}$ and $A0_{t1}$ modes interacting with the second defect, reducing the enhancement that can be observed from the second defect.

When the smaller defect is encountered first, the amplitude of the transmitted waves $A0_{t1}$ and $S0_{t1}$ can be large, and therefore larger magnitude additional reflections can be produced (e.g. $S0_{t1}$-$S0_{r2}$ and $A0_{t1}$-$A0_{r2}$) which contribute to the enhancement at the second defect. This leads to the large enhancement observed at the second defect position in figure 12 when the second defect is deeper than the first. The presence of the smaller initial defect can still be observed by the deviations of the enhancement pattern from the single defect case. To obtain a more complete idea of the defect depths relative to one another a scan can be performed from both directions.

In figure 13, for 5 mm separation, it is possible to determine two different enhancements for all permutations of the two defects; note that the second enhancement occurs in addition to the transmission enhancement peak (centred around 5 mm on figure 7). The separation means that both transmitted modes will still affect the overall enhancement at the second defect, however, both sets of enhancement peaks have the same structure as the single defect enhancements shown in figure 7. An estimate of the defect positions can be made by the location at which the central peaks occur.

The enhancement factor for a single simulated 50% depth defect was found to be 1.72 (figure 8b). For the cases in figure 13a where the first defect encountered is 50% of the sheet thickness, the enhancement from this 50% defect was found to be consistent for the double defect geometry. However, the presence of the initial 50% defect had the effect of increasing the enhancement fac-

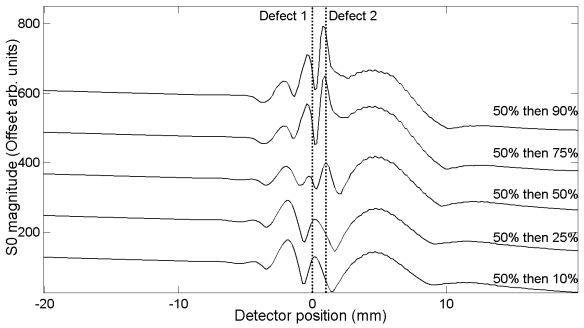

(a)

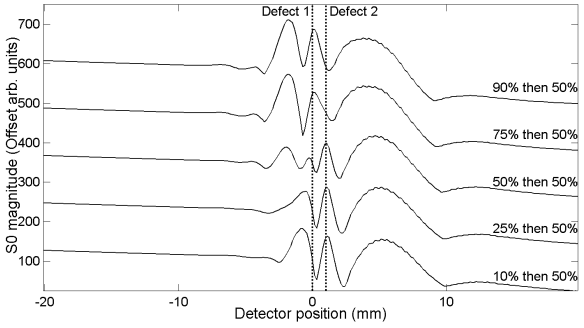

(b)

Figure 12: Variation in the sonogram magnitude of the S0 wave in the region of interest for two hidden defects separated by 1 mm when the detector first encounters a fixed 50% depth defect followed by a defect of varied depth (a), and when the detector encounters the fixed defect second (b).

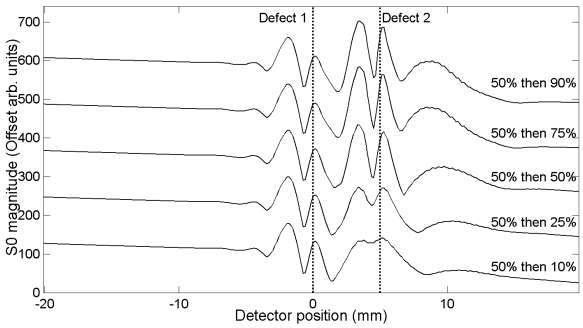

(a)

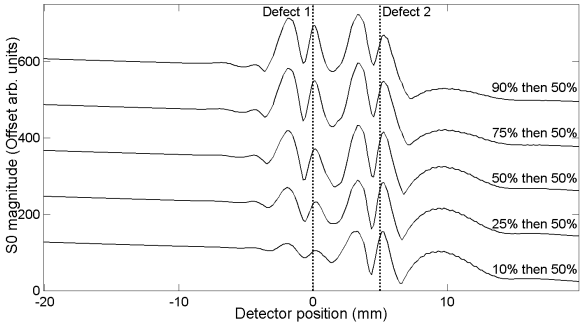

(b)

Figure 13: Variation in the sonogram magnitude of the S0 wave in the region of interest for two hidden defects separated by 5 mm when the detector first encounters a fixed 50% depth defect followed by a defect of varied depth (a), and when the detector encounters the fixed defect second (b).

tors for the second, variable depth defects, due to the presence of the transmission enhancement, with an increase in the enhancement factor from 1.10 to 1.41 for a 10% defect and 2.19 to 2.96 for a 90% defect. The significance of this increased enhancement at the 5 mm separation can be highlighted by comparing the 10% then 50% defect pairings from figures 12 and 13; the smaller defect was undetectable for the 1 mm separation, but clear for the larger separation.

When the 50% depth defect is the second defect encountered the enhancement factor for this defect was found to increase to above the single defect value of 1.72, for the same reason as the increase in enhancement discussed above. A larger increase was seen for a deeper initial defect, with the 50% depth defect enhancement factor increasing to 2.14 for a 10% depth first defect, to 2.58 for a 90% depth first defect. Figure 13 therefore shows that, although enhancement factors can be found for each defect at a separation of 5 mm, the presence of multiple defects can act to alter the magnitude of the observed enhancements when compared to the single defect case. The nature of the changes to the enhancement are dependent upon which defect is encountered first, and so to obtain as much information about the defect system as possible the sample should be scanned from both directions. However, the enhancements can still be used as a guide to approximate the defect sizes, and for separations of 7 mm or larger at this analysis frequency range, when the enhancement patterns are clearly separated, the sizing regains accuracy.

4. Conclusions

It has been shown that near-field ultrasonic enhancement of a fundamental symmetric Lamb wave incident on a hidden defect can be used to position the defect and obtain an estimate of its severity. The successful identification of multiple defects has been shown for two defect systems for a variety of different separations between the defects and for defects of different relative

depths. The near-field scanning technique is especially useful for resolution of individual defects within a defect cluster, which can be difficult to achieve using far-field methods.

The detection of hidden defects by this method is of particular merit when compared to the traditional dye-penetrant approach, which can only be applied to an accessible surface. Higher resolution would be possible by using pulses of higher frequency and shorter time duration, however, care must be taken to avoid increasing the complexity of the signals by allowing the presence of more than just the fundamental S0 and A0 Lamb wave modes. The near-field inspection method could be used in conjunction with a long range guided wave method, where the far-field inspection could be used to provide the approximate location of a defect cluster before the near-field inspection is used to quantify the nature of the defects within that cluster.

Acknowledgments

This work was funded by the European Research Council under grant 202735, NonContactUltrasonic, ERC Starting Independent Researcher Grant.

5. References

References

[1] R A Cottis. Stress corrosion cracking. *NPL*, 2000.

[2] C Manfredi and J L Otegui. Failure by SCC in buried pipelines. *Engineering Failure Analysis*, **9**:pp. 495–509, 2002.

[3] B. Y. Fang, A. Atrens, J. Q. Wang, E. H. Han, Z. Y. Zhu, and W. Ke. Review of stress corrosion cracking of pipeline steels in low and high ph solutions. *Journal of Materials Science*, **8**:pp. 127–132, 2003.

[4] S. G Polyakov and A. A. Rybakov. The main mechanisms of stress corrosion cracking in natural gas trunk lines. *Strength of Materials*, **41**:pp. 456–463, 2009.

[5] A. de Sterke. A practical introduction to penetrants. *Nondestructive Testing*, **1**:pp. 306–307, 1968.

[6] N. P. Migun, A. B. Gnusin, and I. V. Volovich. Some possibilities of enhancing the efficiency of penetrant inspection. *Russian journal of nondestructive testing*, **41**:pp. 452–455, 2005.

[7] A. Maksimenko, M. Ando, H. Sugiyama, and E. Hashimoto. Possibility of computed tomographic reconstruction of cracks from X-ray refraction contrast. *Japanese Journal of Applied Phyiscs*, **44**:pp. 633–635, 2005.

[8] M. J. S. Lowe, D. N. Alleyne, and P. Cawley. Defect detection in pipes using guided waves. *Ultrasonics*, **36**:pp. 147–154, 1998.

[9] P. Cawley and D. N. Alleyne. The use of Lamb waves for the long range inspection of large structures. *Ultrasonics*, **34**:pp. 287–290, 1996.

[10] M. Kobayashi and C-K. Jen. Piezoelectric thick bismuth titanate/lead zirconate titanate composite film transducers for smart NDE of metals. *Smart Materials and Structures*, **13**:pp. 951–956, 2004.

[11] C.B. Scruby and L.E. Drain. *Laser ultrasonics. Techniques and applications*. Adam Hilger, 1990.

[12] M Hirao and H Ogi. *EMATs for science and industry. Noncontacting ultrasonic measurements.* Kluwer Academic Publishers, 2003.

[13] R. J. Dewhurst, C. Edwards, A. D. W. McKie, and S. B. Palmer. A remote laser system for ultrasonic velocity measurement at high temperatures. *Journal of Applied Physics*, **63**:pp. 1225–1227, 1988.

[14] M. Castaings and P. Cawley. The generation, propagation, and detection of Lamb waves in plates using air-coupled ultrasonic transducers. *Journal of the Acoustical Society of America*, **100**: pp. 3070–3077, 1996.

[15] T. Hayashi and M. Murase. Defect imaging with guided waves in a pipe. *Journal of the Acoustical Society of America*, **117**:pp. 2134–2140, 2005.

[16] B. Massarey, C. Raemy, and P. Fromme. High-frequency guided ultrasonic waves for hidden defect detection in multi-layered aircraft structures. *Ultrasonics*, **54(7)**:pp. 1720–1728, 2014.

[17] J. David and N. Cheeke. *Fundamentals and applications of ultrasonic waves.* CRC Press, 2002.

[18] R. S. Edwards, S. Dixon, and X. Jian. Characterisation of defects in the railhead using ultrasonic surface waves. *NDT & E Internationa*, **39(6)**:pp. 469–475, 2006.

[19] A. Lovstad and P. Cawley. The reflection of the fundamental torsional guided wave from multiple circular holes in pipes. *NDT & E International*, **44**:pp. 553–562, 2011.

[20] R. S. Edwards, S. Dixon, and X. Jian. Enhancement of the Rayleigh wave signal at surface defects. *Journal of Physics D: Applied Physics*, **37**:pp. 2291–2297, 2004.

[21] S. Dixon, B. Cann, D. L. Carroll, Y. Fan, and R. S. Edwards. Non-linear enhancement of laser generated Rayleigh waves by cracks. *Nondestrutive Testing and Evaluation*, **23**:pp. 25–34, 2008.

[22] A. R. Clough and R. S. Edwards. Lamb wave near field enhancements for surface-breaking defects in plates. *Journal of Applied Physics*, **111**:p. 104906, 2012.

[23] A. R. Clough and R. S. Edwards. Scanning laser source Lamb wave enhancements for defect characterisation. *NDT & E International*, **62**:pp. 99–105, 2014.

[24] F. Hernandez-Valle, A. R. Clough, and R. S. Edwards. Stress corrosion cracking detection using laser/laser and laser/EMAT techniques. *Corrosion Science*, **78**:pp. 335–342, 2014.

[25] J. L. Rose. *Ultrasonic waves in solid media.* Cambridge University Press, 1999.

[26] M. B. Klein, G. D. Bacher, A. Grunnet-Jepsen, D. Wright, and W. E. Moerner. Homodyne detection of ultrasonic surface displacements using two-wave mixing in photorefractive polymers. *Optics Communications*, **162**:pp. 79–84, 1999.

[27] M. Niethammer, L. J. Jacobs, J. Qu, and J. Jarzynski. Time-frequency representation of Lamb waves. *Journal of the Acoustical Society of America*, **109**:pp. 1841–1847, 2001.

[28] B. Kim and Y. Roh. Simple expression of the reflection and transmission coefficients of fundamental Lamb waves by a rectangular notch. *Ultrasonics*, **51**:pp. 734–744, 2011.

[29] M. Castaings, E. Le Clezio, and B. Hosten. Modal decomposition method for modeling the interaction of Lamb waves with cracks. *Journal of the Acoustical Society of America*, **112**:pp. 2567–2582, 2002.